

# Neutron star properties with careful parametrization in the vector and axial-vector meson extended linear sigma model

Péter Kovács<sup>\*</sup> and János Takátsy

*Institute for Particle and Nuclear Physics, Wigner Research Centre for Physics, 1121 Budapest, Hungary  
and Institute of Physics, Eötvös University, 1117 Budapest, Hungary*

Jürgen Schaffner-Bielich

*Institut für Theoretische Physik, Goethe Universität Frankfurt, D-60438 Frankfurt, Germany*

György Wolf

*Institute for Particle and Nuclear Physics, Wigner Research Centre for Physics, 1121 Budapest, Hungary*



(Received 12 November 2021; accepted 7 April 2022; published 16 May 2022)

The existence of quark matter inside the cores of heavy neutron stars is a possibility which can be probed with modern astrophysical observations. We use a vector and axial-vector meson extended quark-meson model to describe quark matter in the core of neutron stars. We discover that an additional parameter constraint is necessary in the quark model to ensure chiral restoration at high densities. By investigating hybrid star sequences with various parameter sets, we show that low sigma meson masses are needed to fulfill the upper radius constraints and that the maximum mass of stable hybrid stars is only slightly dependent on the parameters of the crossover-type phase transition. Using this observation and results from recent astrophysical measurements, a constraint of  $2.5 < g_V < 4.3$  is set for the constituent quark–vector meson coupling. The effect of a nonzero bag constant is also investigated, and we observe that its effect is small for values adopted in previous works.

DOI: [10.1103/PhysRevD.105.103014](https://doi.org/10.1103/PhysRevD.105.103014)

## I. INTRODUCTION

The theory of strong interaction, QCD, is notoriously difficult to tackle, especially at high but not very high densities or temperatures (around the chiral phase boundary). Although lattice Monte Carlo calculations in the last decades achieved immense progress by solving QCD at low densities and revealing the nature of strongly interacting matter [1,2], the sign problem hinders their application at high densities [3]. On the other hand, perturbative methods only become reliable at very high energies, not relevant for most physical scenarios involving dense nuclear matter [4]. From the experimental side, ALICE at CERN [5] and PHENIX and STAR at RHIC [6,7] also managed to explore QCD at low density and high temperature. Up to this day, experimental data at high densities are scarce and have rather bad statistics [7,8]; however, multiple experimental facilities that are under construction are designed to explore this region with higher precision in the near future [9,10].

One possibility to explore this area is the usage of effective theories, which can be applied at finite density and provide important insight about certain aspects of strongly interacting matter. In our approach, the underlying principle

of constructing such a model is to require that the Lagrangian—involving composite particles (mesons and constituent quarks) instead of the fundamental quarks and gluons—has the same global symmetries as QCD itself. One group of these models consists of chiral effective field theories, which are designed to describe chiral restoration at high temperatures and densities and are expected to be reliable in the vicinity of chiral phase transition.

Recent studies, based on astrophysical measurements in the last few years, argue that deconfined quark matter might also exist inside the core of neutron stars (NSs) and in dense stellar remnants (see, e.g., Refs. [11,12]). The emergence of increasingly robust predictions were made possible by major advances in the observation of NSs in the previous decade, which have already put multiple constraints on the equation of state (EoS) of dense strongly interacting matter. These constraints stem from a variety of astrophysical observations, ranging from the discovery of NSs with masses of  $2 M_\odot$  [13–16], through gravitational-wave measurements of the inspirals of NS-NS systems [17,18], to the x-ray pulse-profile measurements of pulsars with NICER [19–22] together with qualitative improvements in x-ray radius measurements (see, e.g., Ref. [23]).

The chiral mean field model is based on a Yukawa-type scalar and vector meson exchange for nucleons and quarks

\*kovacs.peter@wigner.hu

obeying chiral symmetry [24–29]. The chiral quark-meson model uses the linear sigma model and has been extended by implementing vector meson exchange and a vacuum term [30,31]. As it turned out, both additions to the linear sigma model have a significant impact on the properties of compact star configurations. The quark-meson model has been also investigated for compact stars by going beyond mean-field using renormalization for the quark part [32] and by adopting the functional renormalization group method [33,34]. Confronting recent astrophysical data on NSs with chiral models for quark matter has been also performed within a nonlocal Nambu-Jona-Lasinio model [35–37] and a unified quark-meson-nucleon model [38].

It is still uncertain what kind of matter exists in the core of NSs. At very large chemical potentials, the ground state of the strongly interacting matter is in some color superconducting state [39]; however, the critical density of the transition from ordinary to superconducting matter is not known yet. Furthermore, it is also unknown whether by increasing baryon/quark density the hadronic matter transforms first to ordinary or to superconducting quark matter. In this paper, we consider the situation where in the center of the compact stars ordinary quark matter exists, and the superconducting phase appears at higher densities than could be reached in NS cores. The description of quark matter in connection with NSs has been investigated using various chiral approaches. Specifically, the role of diquark condensate, which accounts for the color superconductivity, is investigated thoroughly in Refs. [40–42], while a more recent work on the subject is Ref. [43].

In this paper, we use a vector and axial-vector meson extended linear sigma model (eLSM) with constituent quarks (or quark-meson model) at zero temperature and finite quark (or baryon) chemical potential to describe the properties of hybrid stars. The advantage of this model—altogether with the parametrization procedure and the approximations that were used—is that it reproduces the meson spectrum (and also various decay widths) quite well at  $T = \mu_q = 0$  [44] and

moreover its finite temperature version also agrees well with various lattice results [45]. Since we think that parametrization plays a crucial role—i.e., depending on the starting position of the parameter space, the system shows very different behavior at finite  $T$  and/or  $\mu_q$ —in the description of properties at finite densities, we investigate the consequences of the asymptotic behavior of the system of equations on the parametrization. It turns out that the system does not behave as expected with every parametrization.

Using two different hadronic models at low densities, we construct hybrid star EoSs, which fulfill all the current expectations coming from astrophysical measurements, providing some of the parameters, like the  $g_V$  vector coupling, are set properly.

The paper is organized as follows. Section II is devoted to the introduction of the model, setup of the  $\beta$ -equilibrium and charge neutrality conditions, calculation of the pressure and field equations, and the parametrization procedure. In Sec. III, the hadronic EoSs and interpolation methods (between the hadronic and the quark EoSs) are demonstrated together with a brief summary on compact star observables. Section IV contains our results, where the EoSs, the  $M - R$  curves, the tidal deformabilities ( $\Lambda$ ), and their dependence on various parameters are analyzed. Finally, we summarize the implications of our work in Sec. V. Some additional details can be found in Appendixes A and B.

## II. VECTOR MESON EXTENDED LINEAR SIGMA MODEL

The Lagrangian of the model is a version of the three flavored vector and axial-vector meson extended linear sigma model introduced in Ref. [44], in which it was thoroughly investigated at zero temperature. A slightly modified version of that model was used for finite temperature investigations in Ref. [45]. Here, we use the latter with an additional vector and axial-vector Yukawa-type term. Consequently, the total Lagrangian of the model reads as

$$\begin{aligned}
\mathcal{L} = & \text{Tr}[(D_\mu M)^\dagger (D_\mu M)] - m_0^2 \text{Tr}(M^\dagger M) - \lambda_1 [\text{Tr}(M^\dagger M)]^2 - \lambda_2 \text{Tr}(M^\dagger M)^2 + c_1 (\det M + \det M^\dagger) + \text{Tr}[H(M + M^\dagger)] \\
& - \frac{1}{4} \text{Tr}(L_{\mu\nu}^2 + R_{\mu\nu}^2) + \text{Tr} \left[ \left( \frac{m_1^2}{2} + \Delta \right) (L_\mu^2 + R_\mu^2) \right] + i \frac{g_2}{2} (\text{Tr}\{L_{\mu\nu}[L^\mu, L^\nu]\} + \text{Tr}\{R_{\mu\nu}[R^\mu, R^\nu]\}) \\
& + \frac{h_1}{2} \text{Tr}(M^\dagger M) \text{Tr}(L_\mu^2 + R_\mu^2) + h_2 \text{Tr}(|L_\mu M|^2 + |MR_\mu|^2) + 2h_3 \text{Tr}(L_\mu MR^\mu M^\dagger) + \bar{\Psi} [i\gamma_\mu D^\mu - \mathcal{M}] \Psi \\
& - g_V \bar{\Psi} \left[ \gamma_\mu V^\mu + \frac{g_A}{g_V} \gamma^5 \gamma_\mu A^\mu \right] \Psi,
\end{aligned} \tag{1}$$

where, as it is described in detail in Ref. [45],  $M = M_S + M_{PS}$ ,  $L^\mu = V^\mu + A^\mu$ ,  $R^\mu = V^\mu - A^\mu$ , and  $M_S, M_{PS}, V^\mu, A^\mu$  stand for the scalar, the pseudoscalar, the vector, and the axial vector nonets, respectively, while  $\Psi = (q_u, q_d, q_s)^T$  stands for the constituent quark fields.

Some comments are in order. There are two new unknown parameters. One is the  $g_V$  vector coupling, which has a direct impact on the value of the maximal mass on the  $M - R$  curve of compact stars. Although the  $g_A$  axial coupling (or the  $g_A/g_V$  ratio) is also unknown, it will

not appear in any of the following expressions; thus, its value is irrelevant for the current investigation. In Ref. [45], we also introduced Polyakov-loop variables, which vanish at zero temperature; thus, they will not be present in the equations relevant for compact stars, but since in the parametrization the pseudocritical temperature is used, it still affects the parameter set.

As a standard procedure for theories with spontaneous symmetry breaking, nonzero vacuum expectation values (VEVs) are assumed for the nonstrange and strange isoscalar fields  $\sigma_N$  and  $\sigma_S$  and for the temporal component of the three vector fields: the charge neutral  $\rho_0^\mu$ ,  $\omega^\mu$ , and  $\Phi^\mu$ . These expectation values are denoted as follows:

$$\begin{aligned} \langle \sigma_N \rangle &\equiv \phi_N, & \langle \sigma_S \rangle &\equiv \phi_S, \\ \langle \rho_0^0 \rangle &\equiv v_\rho, & \langle \omega^0 \rangle &\equiv v_\omega, & \langle \Phi^0 \rangle &\equiv v_\Phi. \end{aligned} \quad (2)$$

It should be noted that we neglect here the small effect of isospin breaking, which would require the introduction of a nonzero expectation value for the scalar  $a_0^0$  field.

Hereafter, the fields are shifted with their nonzero expectation values, which subsequently results in the tree-level expressions for the meson and constituent quark masses and the tree-level decay widths. Moreover, the nonzero vector VEVs shift the  $\mu_u$ ,  $\mu_d$ , and  $\mu_s$  quark chemical potentials of the constituent quark fields, subsequently leading to the following effective quark chemical potentials for the different flavors:

$$\begin{aligned} \tilde{\mu}_u &= \mu_u - \frac{1}{2} g_V (v_\omega + v_\rho), \\ \tilde{\mu}_d &= \mu_d - \frac{1}{2} g_V (v_\omega - v_\rho), \\ \tilde{\mu}_s &= \mu_s - \frac{1}{\sqrt{2}} g_V v_\Phi. \end{aligned} \quad (3)$$

These shifts stem from the vector Yukawa term, which is the last term of the Lagrangian [Eq. (1)].

### A. $\beta$ equilibrium and charge neutrality

We add a free electron gas to our system with some  $\mu_e$  electron chemical potential and assume  $\beta$  equilibrium, which is

$$\mu_d = \mu_s = \mu_u + \mu_e$$

after neutrinos have left the system. Thus, using

$$\mu_q \equiv \frac{1}{3} \mu_B = \frac{1}{3} (\mu_u + \mu_d + \mu_s) \quad (4)$$

for the quark chemical potential, the chemical potentials for the different flavors are given by

$$\begin{aligned} \mu_u &= \mu_q - \frac{2}{3} \mu_e, \\ \mu_d &= \mu_q + \frac{1}{3} \mu_e, \\ \mu_s &= \mu_q + \frac{1}{3} \mu_e. \end{aligned} \quad (5)$$

Charge neutrality is also applied and can be written as

$$\frac{2}{3} n_u - \frac{1}{3} n_d - \frac{1}{3} n_s - n_e = 0, \quad (6)$$

where  $n_{u/d/s}$  and  $n_e$  are the number densities for the  $u$ ,  $d$ ,  $s$  quarks and the electron, respectively. They can be calculated as

$$n_f = \frac{\partial p}{\partial \mu_f}, \quad f \in (u, d, s), \quad n_e = \frac{\partial p}{\partial \mu_e}, \quad (7)$$

where  $p$  is the pressure.

Finally, the effective quark chemical potentials for the different flavors can be written as

$$\begin{aligned} \tilde{\mu}_u &= \mu_q - \frac{2}{3} \mu_e - \frac{1}{2} g_V (v_\omega + v_\rho), \\ \tilde{\mu}_d &= \mu_q + \frac{1}{3} \mu_e - \frac{1}{2} g_V (v_\omega - v_\rho), \\ \tilde{\mu}_s &= \mu_q + \frac{1}{3} \mu_e - \frac{1}{\sqrt{2}} g_V v_\Phi. \end{aligned} \quad (8)$$

It should be noted here that, while  $\mu_{u/d/s}$  play the role of the usual chemical potentials, in the calculation of the grand potential (or the pressure) the  $\tilde{\mu}_{u/d/s}$  effective chemical potentials appear.

### B. Pressure and the field equations

The pressure is given by

$$p(\mu_f, \mu_e) = \Omega_0 - \Omega(T=0, \mu_f, \mu_e), \quad (9)$$

where  $\Omega$  is the grand potential. The grand potential is calculated in a hybrid approximation used in Ref. [45] at zero temperature with additional vector condensates introduced above. In this hybrid approach, we consider only quark fluctuations, while all the mesons are at tree level. The grand potential consist of the terms

$$\Omega_{\text{tot}} = U_{\text{meson}}(\phi_N, \phi_S, v_\rho, v_\omega, v_\Phi) + \Omega_{qq}^{\text{vac}} + \Omega_{qq}^{\text{mat}}(\mu_f) + \Omega_{\text{el}}, \quad (10)$$

where  $U_{\text{meson}}$  stands for the tree-level meson potential,  $\Omega_{qq}^{\text{vac}}$  and  $\Omega_{qq}^{\text{mat}}$  stand for the vacuum and matter part of the

one-loop constituent quark contributions, and  $\Omega_{el}$  stands for the electron contribution. Its explicit form can be found in Eq. (A1) of Appendix A. The field equations are the stationary points of the grand potential, i.e.,

$$\frac{\partial\Omega_{\text{tot}}}{\partial\phi_N} = \frac{\partial\Omega_{\text{tot}}}{\partial\phi_S} = \frac{\partial\Omega_{\text{tot}}}{\partial v_\omega} = \frac{\partial\Omega_{\text{tot}}}{\partial v_\rho} = \frac{\partial\Omega_{\text{tot}}}{\partial v_\Phi} = 0. \quad (11)$$

These are five coupled equations for the  $\mu_q$  (or  $\mu_B$ ) dependence of the scalar and vector condensates. There is another unknown, the  $\mu_e$  electron chemical potential, which is determined through the charge neutrality condition, which is also coupled to the preceding five equations. The explicit form of the system of six equations that needs to be solved reads as

$$\begin{aligned} \frac{\partial\Omega_{\text{tot}}}{\partial\phi_N} = & m_0^2\phi_N + \lambda_1(\phi_N^2 + \phi_S^2)\phi_N + \frac{1}{2}\lambda_2\phi_N^3 - \frac{c_1}{\sqrt{2}}\phi_N\phi_S - h_N - \frac{1}{2}(h_1 + h_2 + h_3)\phi_N(v_\omega^2 + v_\rho^2) - \frac{1}{2}h_1\phi_Nv_\Phi^2 \\ & - \frac{3g_F}{8\pi^2}m_u^3 \left[ 1 + 4 \log \frac{m_u}{M_0} \right] + \frac{3g_F}{4\pi^2} \sum_{f \in (u,d)} m_f^3 \left[ \gamma_f \sqrt{\gamma_f^2 - 1} - \log \left( \gamma_f + \sqrt{\gamma_f^2 - 1} \right) \right] = 0 \end{aligned} \quad (12)$$

$$\begin{aligned} \frac{\partial\Omega_{\text{tot}}}{\partial\phi_S} = & m_0^2\phi_S + \lambda_1(\phi_N^2 + \phi_S^2)\phi_S + \lambda_2\phi_S^3 - \frac{c_1}{2\sqrt{2}}\phi_N^2 - h_S - \frac{1}{2}h_1\phi_S(v_\omega^2 + v_\rho^2) - \frac{1}{2}(h_1 + 2h_2 + 2h_3)\phi_Sv_\Phi^2 \\ & - \frac{3g_F}{8\sqrt{2}\pi^2}m_s^3 \left[ 1 + 4 \log \frac{m_u}{M_0} \right] + \frac{3g_F}{2\sqrt{2}\pi^2}m_s^3 \left[ \gamma_s \sqrt{\gamma_s^2 - 1} - \log \left( \gamma_s + \sqrt{\gamma_s^2 - 1} \right) \right] = 0 \end{aligned} \quad (13)$$

$$\frac{\partial\Omega_{\text{tot}}}{\partial v_\omega} = -m_\rho^2v_\omega + \frac{m_u^3}{2\pi^2}g_V \sum_{f \in (u,d)} \text{sgn}(\tilde{\mu}_f)(\gamma_f^2 - 1)^{\frac{3}{2}} = 0 \quad (14)$$

$$\frac{\partial\Omega_{\text{tot}}}{\partial v_\rho} = -m_\rho^2v_\rho + \frac{m_u^3}{2\pi^2}g_V [\text{sgn}(\tilde{\mu}_u)(\gamma_u^2 - 1)^{\frac{3}{2}} - \text{sgn}(\tilde{\mu}_d)(\gamma_d^2 - 1)^{\frac{3}{2}}] = 0 \quad (15)$$

$$\frac{\partial\Omega_{\text{tot}}}{\partial v_\Phi} = -m_\Phi^2v_\Phi + \frac{m_s^3}{\sqrt{2}\pi^2}g_V \text{sgn}(\tilde{\mu}_s)(\gamma_s^2 - 1)^{\frac{3}{2}} = 0 \quad (16)$$

$$2\text{sgn}(\tilde{\mu}_u)(\tilde{\mu}_u^2 - m_u^2)^{\frac{3}{2}} - \text{sgn}(\tilde{\mu}_d)(\tilde{\mu}_d^2 - m_d^2)^{\frac{3}{2}} - \text{sgn}(\tilde{\mu}_s)(\tilde{\mu}_s^2 - m_s^2)^{\frac{3}{2}} - \text{sgn}(\mu_e)(\mu_e^2 - m_e^2)^{\frac{3}{2}} = 0, \quad (17)$$

where  $\gamma_f$  is defined in Eq. (A4), while the  $m_\rho = m_\omega$ , and  $m_\Phi$  masses are given in Eqs. (A2) and (A3). It should be noted that each term that contains  $\sqrt{\gamma_f^2 - 1}$  or  $\sqrt{\tilde{\mu}_f^2 - m_f^2}$  is only present if  $\tilde{\mu}_f > m_f$ .

### C. Model parameters and asymptotic behavior of the equations

To solve our system of equations [Eqs. (12)–(17)] at finite  $\mu_q$ , the parameters of the model should be determined first. The 15 unknown parameters are  $m_0, \lambda_1, \lambda_2, c_1, m_1, g_1, g_2, h_1, h_2, h_3, \delta_S, \phi_N, \phi_S, g_F$ , and  $g_V$ . As described in detail in Sec. IV. of [45], we calculate meson masses and decay widths at  $\mu_q = T = 0$  and compare them to their experimental value—taken from the (Particle Data Group) PDG [46]—through a  $\chi^2$  fit. Moreover, we also calculate the pseudocritical temperature  $T_c$  at  $\mu_q = 0$  and compare to the value 150 MeV, which was taken from the lattice [47,48]. It should be noted that lately the value for  $T_c$  was updated to

$156.5 \pm 1.5$  MeV [49]; however, from the perspective of the current investigation, this difference of  $\sim 7$  MeV is negligible. Since in the current approximation we use tree-level vector and axial-vector masses, the  $g_V$  vector coupling does not appear in any of the expressions; thus, it remains a free parameter. It should be noted, however, that if we include fermionic fluctuations in the curvature masses of the vectors and axial-vectors  $g_V$  will also be fixed through the  $\chi^2$  minimization [50].

During the investigation of different parameter sets, we noticed some unusual behavior of the  $\phi_{N/S}$  scalar condensates as a function of  $\mu_q$ , namely, for large  $\mu_q$  values  $\phi_{N/S}$  started to increase substantially, as shown in Fig. 1. This behavior would mean the recurrence of chiral symmetry breaking for large  $\mu_q$ , which seems unphysical. It should be emphasized here that this behavior is due to the introduction of nonzero vector condensates, and therefore in previous investigations [44,45,50], this problem did not occur.

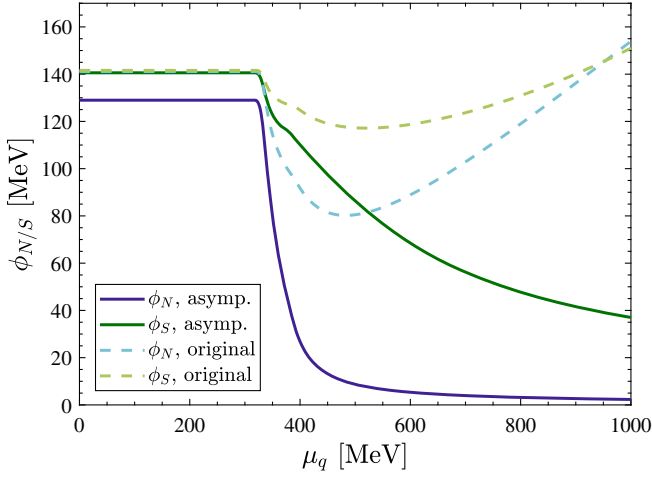


FIG. 1. The dependence of the  $\phi_{N/S}$  scalar condensates on the quark chemical potential with (solid lines) and without (dashed lines) the asymptotic condition of Eq. (30). The parameter sets for these results are shown in Table I and in Table IV of Ref. [45], and  $g_V = 5$  in both cases. This shows that a naive parametrization of the model results in an increase of the scalar condensates at higher densities and therefore the recurrence of chiral symmetry breaking.

In other words, with the introduction of vector condensates, it is necessary to change the model parameters.

To avoid this unwanted behavior, we investigated the asymptotic solution for large  $\mu_q$  and demanded the disappearance of the  $\phi_{N/S}$  condensates at these asymptotic values. Thus, more explicitly, it is assumed that for large  $\mu_q$

$$\begin{aligned} \phi_N &\sim \mu_q^{-\alpha}, & \phi_S &\sim \mu_q^{-\beta}, \\ v_\omega &\sim \mu_q^k, & v_\rho &\sim \mu_q^l, & v_\Phi &\sim \mu_q^n, \end{aligned} \quad \text{with } \alpha, \beta, k, l, n \geq 0. \quad (18)$$

It is also assumed that  $\tilde{\mu}_{u/d/s} > 0$ . With these assumptions in leading order,

$$\begin{aligned} \text{sgn}(\tilde{\mu}_f) m_f^3 (\gamma_u^2 - 1)^{\frac{3}{2}} &\approx \tilde{\mu}_f^3, \\ m_{\omega/\rho/\Phi}^2 &\approx m_1^2. \end{aligned}$$

Consequently, Eqs. (14)–(17) will have the forms—neglecting the electron’s mass as well,

$$m_1^2 v_\omega \approx \frac{g_V}{2\pi^2} (\tilde{\mu}_u^3 + \tilde{\mu}_d^3), \quad (19)$$

$$m_1^2 v_\rho \approx \frac{g_V}{2\pi^2} (\tilde{\mu}_u^3 - \tilde{\mu}_d^3), \quad (20)$$

$$m_1^2 v_\Phi \approx \frac{g_V}{\sqrt{2}\pi^2} \tilde{\mu}_s^3, \quad (21)$$

$$\mu_e^3 \approx 2\tilde{\mu}_u^3 - \tilde{\mu}_d^3 - \tilde{\mu}_s^3. \quad (22)$$

Rearranging Eq. (21) and substituting Eqs. (8) for  $\tilde{\mu}_s$ , it can be written that

$$\frac{g_V}{\sqrt{2}\pi^2} \left( \mu_q + \frac{1}{3}\mu_e - \frac{1}{\sqrt{2}}g_V v_\Phi \right)^3 - m_1^2 v_\Phi \approx 0, \quad (23)$$

where the first part of the left-hand side is a third-order polynomial in  $v_\Phi$  that scales with  $\sim \mu_q^{3n}$ ; thus, the second term  $m_1^2 v_\Phi$  which scales only with  $\sim \mu_q^n$  can be neglected compared to that since  $n \geq 0$ . Consequently, the expression in the parentheses—which is simply  $\tilde{\mu}_s$ —is zero in leading order ( $\tilde{\mu}_s \approx 0$ ). Similar arguments lead to  $\tilde{\mu}_u \approx 0$ ,  $\tilde{\mu}_d \approx 0$ . Accordingly, from Eq. (22), we conclude that  $\mu_e \approx 0$ . Thus, the effective quark chemical potentials for the flavors in leading order are zero,

$$\tilde{\mu}_u \approx 0, \quad \tilde{\mu}_d \approx 0, \quad \tilde{\mu}_s \approx 0, \quad \mu_e \approx 0. \quad (24)$$

Using Eq. (8) in Eqs. (24) and rearranging for the vector condensates results in

$$v_\omega \approx \frac{2}{g_V} \mu_q \quad (25)$$

$$v_\rho \approx 0 \quad (26)$$

$$v_\Phi \approx \frac{\sqrt{2}}{g_V} \mu_q. \quad (27)$$

Using these approximations in Eq. (12) gives

$$-h_N - \frac{1}{2}(h_1 + h_2 + h_3)\phi_N \frac{4}{g_V^2} \mu_q^2 - \frac{1}{2}h_1 \phi_N \frac{2}{g_V^2} \mu_q^2 \approx 0. \quad (28)$$

Expressing  $\phi_N$  finally results in

$$\phi_N = -\frac{h_N g_V^2}{3h_1 + 2h_2 + 2h_3} \mu_q^{-2}. \quad (29)$$

Since  $\phi_N > 0$ , and  $h_N > 0$ , this implies the following condition:

$$3h_1 + 2h_2 + 2h_3 < 0. \quad (30)$$

Investigating the asymptotic behavior of Eq. (13) for  $\phi_S$  leads to the same condition. Consequently, the asymptotic exponents of the condensates are

$$\alpha = \beta = 2, \quad k = n = 1, \quad l = 0. \quad (31)$$

Note that we also checked this numerically with different parametrizations and found that the condition in (30) is valid.

It is worth it to note that to reach that conclusion we assumed in Eq. (18) that  $k$ ,  $l$ , and  $n$  exponents are

TABLE I. Parameter values for  $m_\sigma = 290$  MeV.

Parameter	Value	Parameter	Value
$\phi_N$ (GeV)	0.1290	$g_1$	5.3296
$\phi_S$ (GeV)	0.1406	$g_2$	-1.0579
$m_0^2$ (GeV <sup>2</sup> )	-1.2370 <sub>E-2</sub>	$h_1$	5.8467
$m_1^2$ (GeV <sup>2</sup> )	0.5600	$h_2$	-12.3456
$\lambda_1$	-1.0096	$h_3$	3.5755
$\lambda_2$	25.7328	$g_F$	4.9571
$c_1$ (GeV)	1.4700	$M_0$ (GeV)	0.3935
$\delta_S$ (GeV <sup>2</sup> )	0.2305		

all non-negative. Let us now assume, for instance, that, contrary to that,  $n < 0$ . In this case, in  $\tilde{\mu}_s$  [Eq. (8)], the  $v_\Phi$  term could be neglected compared to  $\mu_q$ , and we would end up with  $m_1^2 v_\Phi \approx \frac{g_V}{\sqrt{2}\pi^2} (\mu_q + 1/3\mu_e)^3$ , where the left-hand side tends to zero, while the right-hand side tends to infinity. Similarly, the assumptions  $k < 0$  or  $l < 0$  would also result in contradictions.

We should add that, although with this condition the scalar condensates tend to zero at asymptotically large densities, they can still show an increase at intermediately large densities where the asymptotic behavior does not yet apply. However, this only happens at large densities, which are not present inside NSs and where our model would already lose its predictive power.

Returning to the determination of the parameters, we use the same procedure as described in Ref. [45] with the additional condition of Eq. (30). The resulting parameter set is given in Table I.

In this case, the  $\sigma$  (or  $f_0$ ) mass is quite low, namely,  $m_\sigma = 290$  MeV. We may also study the dependence of our results on the  $\sigma$  mass, since our fit prefers a rather small value for that, and experimentally it is not very well defined either. Indeed, it is a very broad resonance:  $m_{f_0(500)} = 400$  to  $800$  MeV,  $\Gamma_{f_0(500)} = 100$  to  $800$  MeV [46]. For any chosen  $\sigma$  mass, we have to find a parameter set, which reproduces that value. To achieve this, we have increased the contribution of the  $\sigma$  mass to the  $\chi^2$  by a factor of 1000. This way, by minimizing the  $\chi^2$ , the obtained fit reproduces the prescribed  $\sigma$  mass with less than 0.2% error. The resulting parameter sets can be found in Appendix B.

### III. COMPACT STARS

#### A. Hadronic equation of state

To be able to construct the sequence of stable NSs, we need a reliable equation of state covering many orders of magnitude in density from subsaturation densities up to about  $n \approx 5-6n_0$ , with  $n_0$  being the nuclear saturation density. Below saturation, nuclear methods such as hadron resonance gas models [51,52] and chiral effective field theories [53,54] offer a robust way for describing nuclear matter. The uncertainties of chiral effective field theories

TABLE II. Nuclear properties of symmetric nuclear matter described by the SFHo and DD2 RMF models as well as some properties of NSs described by these models.

Property	SFHo	DD2
Saturation density, $n_0$ (fm <sup>-3</sup> )	0.16	0.15
Binding energy per baryon, $E_0$ (MeV)	-16.17	-16.02
Compressibility, $K_0$ (MeV)	245.2	242.7
Symmetry energy, $S_0$ (MeV)	31.2	32.73
Slope of symmetry energy, $L$ (MeV)	45.7	57.94
Maximum mass neutron star ( $M_\odot$ )	2.06	2.42
Radius of $M = 1.4 M_\odot$ neutron star (km)	11.97	13.26

mainly stem from the truncation of the nuclear Hamiltonian within the expansion, as well as the regularization scheme and scale, resulting in the margins of error for the pressure in state-of-the-art models increasing rapidly above  $n \approx 2n_0$  [55]. Looking at the other side of the density spectrum, at extremely high densities, we expect QCD to become asymptotically free, thus enabling the use of perturbative QCD (pQCD) calculations [56]. However, these methods are only reliable at densities much higher than the ones expected to be present in the center of the most massive NSs. Nevertheless, the EoS of quark matter models should converge to those obtained from pQCD calculations at asymptotically high densities.

In the intermediate-density region, therefore, no fully reliable theory exists, and indeed there is a large selection of nuclear theories using various approaches that range from variational methods to relativistic mean field (RMF) theories [57], which results in a high variation in the calculated nuclear EoSs. These approaches are all based on extrapolations from experimentally measurable nuclear properties at saturation. The most important of these quantities are the binding energy per nucleon ( $E_0 \approx -16.3$  MeV), compressibility ( $K_0 = 240 \pm 20$  MeV), symmetry energy ( $S_0 = 31.6 \pm 2.7$  MeV), and the slope of symmetry energy ( $L = 58.9 \pm 16$  MeV) [58–61].

We use two RMF models, the Steiner-Fischer-Hempel (SFHo) model [62] and the density-dependent RMF model of Typel *et al.* (DD2) [63,64]. They are both consistent with the aforementioned nuclear constraints, the only major difference being the different values for the slope of the symmetry energy  $L$ . This results in the DD2 EoS being stiffer than the SFHo EoS. Some basic properties of the two models are included in Table II. We assume NSs have hadronic crusts described by the EoSs of Baym *et al.* [65] and Negele and Vautherin [66].

#### B. Hadron–quark phase transition

Since the hadronic and quark phases are described by qualitatively different models, we need to match them “by hand” and find an appropriate interpolation method to fix the EoS at intermediate densities. One method uses a simple Maxwell construction, assuming that the hadronic

and quark models describe strongly interacting matter correctly below/above the phase transition point, where  $p_H(\mu_B) = p_Q(\mu_B)$ . This construction results in a first-order phase transition and is limited to cases where the hadronic EoS is stiffer than the quark EoS.

Instead of the Maxwell construction, here we use two methods that interpolate between the hadronic and quark EoSs on a finite density range and hence result in crossover phase transitions. The idea of a smooth interpolation can be supported by the argument that both models lose their validity in the intermediate density region, and therefore a strict extrapolation of the two EoSs is generally not justified.

One of these methods interpolates between the pressures,  $p(\mu_B)$ , on a finite range of chemical potential (see, e.g., Refs. [67,68]). Here, the hadronic EoS is restricted to the domain below  $\mu_{BL}$ , and the quark EoS is restricted to the domain above  $\mu_{BU}$ . These chemical potentials correspond to baryon number densities  $n_L$  and  $n_U$ , respectively. In the intermediate region, a reasonable choice for the interpolating function is a polynomial that smoothly connects the two parts,

$$p(\mu_B) = \sum_{m=0}^N C_m \mu_B^m, \quad \mu_{BL} < \mu_B < \mu_{BU}, \quad (32)$$

where  $C_m$  are coefficients that we may fix by matching the pressure and its derivatives at the boundary points. We use a fifth-order polynomial and match the pressure, the number density, and the sound speed at both boundary points (this is equivalent to matching the pressure together with its first and second derivatives).

The energy density interpolation method, introduced in Ref. [69], applies a smooth interpolation between the  $\varepsilon(n_B)$  curves,

$$\varepsilon(n_B) = \varepsilon_H(n_B)f_-(n_B) + \varepsilon_Q(n_B)f_+(n_B), \quad (33)$$

where  $f_{\pm}$  are hyperbolic tangent interpolating functions,

$$f_{\pm}(n_B) = \frac{1}{2} \left( 1 \pm \tanh \left( \frac{n_B - \bar{n}_B}{\Gamma} \right) \right), \quad (34)$$

with  $\bar{n}_B$  and  $\Gamma$  parametrizing the center and width of the phase transition. The pressure can then be calculated from the thermodynamic relation  $p = n_B^2 \partial(\varepsilon/n_B)/\partial n_B$ . This induces the following expression

$$p(n_B) = p_H(n_B)f_-(n_B) + p_Q(n_B)f_+(n_B) + \Delta p, \quad (35)$$

with

$$\Delta p = n_B(p_H(n_B) - p_Q(n_B))g(n_B), \quad (36)$$

$$g(n_B) = \frac{1}{2\Gamma} \cosh^{-2} \left( \frac{n_B - \bar{n}_B}{\Gamma} \right). \quad (37)$$

Both methods enable us to set the onset and length of the phase transition, which grants us additional degrees of freedom compared to a Maxwell construction. On the other hand, the applicability of these methods is also constrained to a limited range of parameters, since unphysical EoSs may also appear, where the sound speed exceeds unity or the energy density decreases with increasing chemical potential.

One might argue that with mixing the low- and high-density EoSs the energy density interpolation does not fulfill the initial premise of having a simple interpolating function in the intermediate region where both EoSs are unreliable. However, other than a philosophical standpoint, there should be no significant practical difference between this method and any other concatenation of the two EoSs. Nevertheless, as will be shown in Sec. IV C, one should be cautious about using the energy density interpolation and check for a correct low-density behavior.

Throughout our investigation, we will use the SFHo EoS together with the energy density interpolation as our standard choice to construct hybrid stars, although we will investigate the effect of using different hadronic EoSs and concatenation methods in Sec. IV C.

### C. Compact star observables

NS masses and radii can be obtained from general relativistic calculations. The line element for a spherically symmetric configuration can be expressed the following way:

$$ds^2 = e^{\nu(r)} dt^2 - e^{\lambda(r)} dr^2 - r^2(d\theta^2 + \sin^2\theta d\varphi^2). \quad (38)$$

Assuming that the matter inside NSs can be considered an approximately spherically symmetric perfect fluid with zero temperature, and introducing the variable  $m(r)$  as

$$e^{\lambda(r)} = \left[ 1 - \frac{2m(r)}{r} \right]^{-1}, \quad (39)$$

we can obtain the Tolman-Oppenheimer-Volkoff equations [70,71]

$$\frac{dm(r)}{dr} = 4\pi r^2 \varepsilon(r), \quad (40)$$

$$\frac{dp(r)}{dr} = -[\varepsilon(r) + p(r)] \frac{m(r) + 4\pi r^3 p(r)}{r^2 - 2m(r)r}, \quad (41)$$

where  $p(r)$  is the pressure related to the energy density  $\varepsilon(r)$  by the EoS. Generally, these equations are integrated numerically, and the boundary conditions  $\varepsilon(r=0) = \varepsilon_c$ ,  $p(R) = 0$ , and  $m(R) = M$  determine the total mass ( $M$ ) and radius ( $R$ ) of the NS for a certain central energy density  $\varepsilon_c$ . Varying this energy density creates a sequence of NSs, and thus we obtain the  $M - R$  relation for the specific EoS.

Ideally, one would measure the masses and radii of NSs and hence gradually constrain the  $M - R$  curve and the nuclear EoS. Unfortunately, NS radii are extremely difficult to measure precisely, and up until now, the most accurate measurements managed to achieve an accuracy of  $\sim 10\%$ , meaning  $\sim 1-1.5$  km. The masses of NSs in binary systems, however, can be measured with remarkable precision, and in fact, the most robust constraints originate from the measurements of the most massive NSs. The most massive pulsar known so far, PSR J0740 + 6620, has a mass of  $2.08 \pm 0.07 M_\odot$ , with a 95.4% lower bound of  $1.95 M_\odot$  [16]. This constraint gives a powerful lower limit on the stiffness of the EoS.

Gravitational waves (GW) provide an independent way to observe NSs through their inspiral and merger with another compact object. In the final stages of the inspiral, NSs are distorted through tidal interactions, and this shifts the phase of the emitted GW signal. One of the measurable parameters of NS-NS mergers is the dimensionless quadrupole tidal deformability parameter  $\Lambda = \lambda/M^5$ , with the  $\lambda$  tidal deformability being related to the  $l = 2$  tidal Love number:

$$k_2 = \frac{3}{2} \lambda R^{-5}. \quad (42)$$

Allowing small perturbations on the spherical metric, one can show that  $k_2$  can be expressed the following way [72–75],

$$\begin{aligned} k_2 = & \frac{8}{5} (1 - 2\beta)^2 \beta^5 [2\beta(y_R - 1) - y_R + 2] \\ & \times \{2\beta[4(y_R + 1)\beta^4 + (6y_R - 4)\beta^3 + (26 - 22y_R)\beta^2 \\ & + 3(5y_R - 8)\beta - 3y_R + 6] + 3(1 - 2\beta)^2 \\ & \times [2\beta(y_R - 1) - y_R + 2] \ln(1 - 2\beta)\}^{-1}, \end{aligned} \quad (43)$$

where  $\beta = M/R$  is the compactness parameter of the NS and  $y_R = y(R) = [rH'(r)/H(r)]_{r=R}$  with  $H(r)$  being a function related to the quadrupole metric perturbation.  $y_R$  can be obtained by solving the following first-order differential equation

$$\begin{aligned} ry'(r) + y(r)^2 + r^2 Q(r) \\ + y(r)e^{\lambda(r)} [1 + 4\pi r^2 (p(r) - \varepsilon(r))] = 0, \end{aligned} \quad (44)$$

where

$$\begin{aligned} Q(r) = & 4\pi e^{\lambda(r)} \left( 5\varepsilon(r) + 9p(r) + \frac{\varepsilon(r) + p(r)}{c_s^2(r)} \right) \\ & - 6 \frac{e^{\lambda(r)}}{r^2} - (\nu'(r))^2. \end{aligned} \quad (45)$$

Here,  $c_s^2 = dp/d\varepsilon$  is the sound speed squared, while  $\nu'(r)$  is given by

$$\nu'(r) = \frac{2[m(r) + 4\pi r^3 p(r)]}{r^2 - 2m(r)r}. \quad (46)$$

The first analysis of GW170817 performed by the LIGO-Virgo Collaboration (LVC) inferred a value of  $\Lambda < 800$  for  $1.4 M_\odot$  NSs in the low-spin limit [76]. A thorough investigation of this constraint performed by Annala *et al.* using a generic family of EoSs found an upper radius limit of 13.6 km for  $1.4 M_\odot$  NSs [77], while Most *et al.* arrived at a radius limit of 13.7 km with higher statistics [78]. A subsequent study was also performed by the LVC, in which a combined analysis of tidal deformabilities and NS radii was performed, utilizing various assumptions for the EoSs. Here, the values of  $\Lambda(1.4 M_\odot) = 190_{-120}^{+390}$  and  $R(1.4 M_\odot) = 10.8_{-1.7}^{+2.0}$  km were found [79]. An additional assumption of this study was to use a single EoS to describe both objects, whereas in Ref. [76], the two EoSs were varied independently. A similar study, also using a single EoS ansatz, was performed by De *et al.*, who arrived at a slightly higher upper limit [80] ( $\Lambda < 642$ ,  $\Lambda < 698$  or  $\Lambda < 681$  depending on the prior assumption on the component masses). A companion study of Ref. [79] was also published by the LVC at around the same time, where an EoS agnostic approach was applied [81]. In their study, they investigated the effect of using various waveform templates, and under minimal assumptions, they found for the upper limit of the tidal deformability  $\Lambda(1.4 M_\odot) < 720$  [81].

In this paper, we chose to use the upper limit of  $\Lambda(1.4 M_\odot) < 720$ . We do so since this result was obtained by applying minimal prior assumptions and therefore it sets a conservative upper limit for the tidal deformability. Other, recent studies also use this constraint (e.g., Ref. [82]). Reference [83] examines previous studies [79–81,84,85] and investigates the impact of prior assumptions and argues that upper and especially lower limits on  $\Lambda$  can be misleading without a more detailed discussion. Another reanalysis has also been done by Dietrich *et al.*, which found similar upper limits for  $\Lambda$  (see Table S2 of Ref. [86]).

The electromagnetic properties of the source of GW170817 were also used to put constraints on NSs. A lower radius constraint was inferred by Bauswein *et al.* from the absence of prompt collapse during this event [87], while an upper mass limit of  $2.16_{-0.15}^{+0.17} M_\odot$  was proposed by Rezzolla *et al.* using a quasiuniversal relation between the maximum mass of static and uniformly rotating NSs [88].

X-ray pulse profile measurements of millisecond pulsars also provide additional constraints directly on the masses and radii of pulsars. So far, two pulsars were measured by the NICER Collaboration, one having a typical mass (PSR J0030 + 0451) and the most massive known pulsar (PSR J0740 + 6620) [19–22]. Even though the measurement errors for these pulsars are sizeable, they still manage to rule out a number of EoSs; see, e.g., Refs. [82,89].

Several studies exist that combine these astrophysical measurements with nuclear physics and heavy-ion data to give stringent constraints on the nuclear EoS and the  $M - R$  relation of NSs (e.g., Refs. [85,90,91]). In principle, these constraints should be respected by all EoSs that are allowed by all these conditions separately.

#### IV. RESULTS

Solving simultaneously the system of six equations [Eqs. (12)–(17)] for some parameter set, we get the  $\mu_q$  quark chemical potential dependence of all the condensates. In Fig. 2, the  $\phi_{N/S}$  condensates are shown as a function of  $\mu_q$  for different values of the  $g_V$  vector coupling. For lower  $g_V$  values, an unstable part is present, causing a first-order phase transition, which disappears for larger vector couplings. If the phase transition is of first order at  $T = 0$  as a function of  $\mu_B (= 3\mu_q)$ , then there is a critical end point (CEP) somewhere on the chiral phase boundary on the  $T - \mu_B$  plane. Since, as it is known and will also be seen here, nonzero vector coupling is needed in order to fulfill the two solar mass criteria for the  $M(R)$  curves, it seems that if  $g_V \gtrsim 3.1$  (for  $m_\sigma = 290$  MeV) in this framework the existence of a CEP is unlikely. This is based on the observation that if in a linear sigma model the phase transition is not of first order as a function of  $\mu_B$  at  $T = 0$  then there is no CEP on the  $T - \mu_B$  plane (see, e.g., Ref. [92]).

##### A. Equation of state with different vector couplings and compact star properties

Along the solution [of Eqs. (12)–(17)], the pressure  $p$  [Eq. (9)] and its derivatives can be calculated, from which

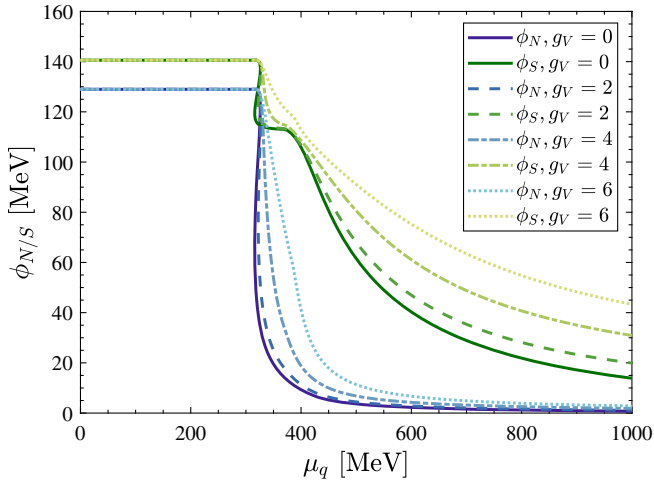


FIG. 2. The chemical potential dependence of the  $\phi_N$  (blue) and  $\phi_S$  (green) scalar condensates. The parameter set with  $m_\sigma = 290$  MeV was used for each curve. Increasingly bright tones correspond to increasing vector couplings of 0 (solid), 2 (dashed), 4 (dot-dashed), and 6 (dotted).

one can construct the EoS. The EoS, which is the pressure as the function of the energy density  $\varepsilon$ , can be seen in Fig. 3 for the SFHo hadronic model, for the pure quark, and for the hybrid stars for two different values of  $g_V$ . For the case  $g_V = 0$ , the hybrid EoS smoothly connects the hadronic and quark phases. However, for the case  $g_V = 5$ , even though the quark EoS is softer than the hadronic one, an intermediate region appears where the hybrid EoS becomes stiffer than both the quark and the hadronic ones. This results in an increase of the maximum compact star mass (see Fig. 4). We note that this behavior is not the consequence of the specific choice for the concatenation method, since it appears for the  $p(\mu)$  interpolation as well (see the comparison of the concatenation methods in Sec. IV C). The same results were reported already in

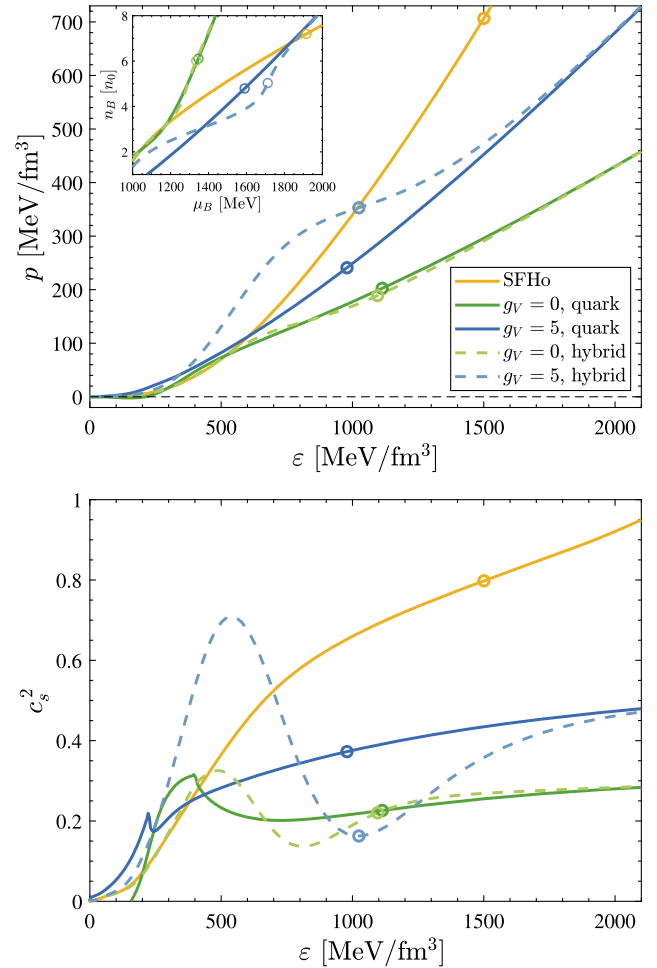


FIG. 3. Top: the EoS ( $p$  as a function of  $\varepsilon$ ) of the SFHo model (yellow solid line), as well as for quark (solid) and hybrid (dashed) stars using the eLSM with the parameter set corresponding to  $m_\sigma = 290$  MeV and vector couplings  $g_V = 0$  (green) and  $g_V = 5$  (blue). The inset contains the same curves for the  $n_B(\mu_B)$  dependence, while the circles correspond to the central conditions inside the maximum mass NSs. For the hybrid EoSs, the energy density interpolation was used with  $\bar{n}_B = 3.5n_0$  and  $\Gamma = 1.5n_0$ . Bottom: the speed of sound squared for the same EoSs.

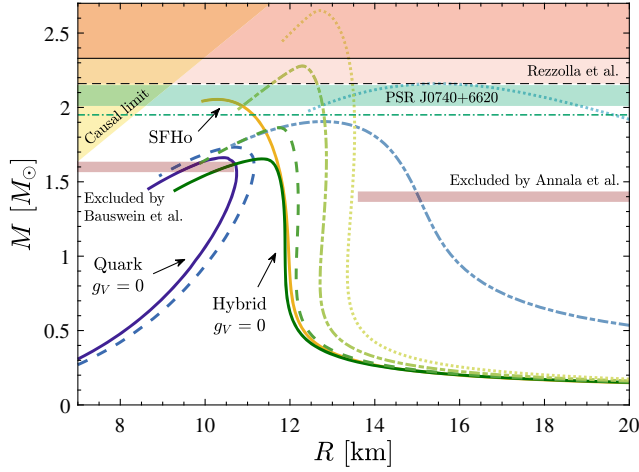


FIG. 4.  $M - R$  relations for the SFHo model (yellow) and for different quark (blue) and hybrid (green) EoSs. Increasingly bright tones correspond to increasing vector couplings of 0 (solid), 2 (dashed), 4 (dot-dashed), and 6 (dotted). The different shaded areas correspond to the lower and upper radius constraints of Bauswein *et al.* [87] and Annala *et al.* [77], respectively; different credibility limits of the upper mass constraint of Rezzolla *et al.* [88]; and the mass of PSR J0740 + 6620 with the 95.4% lower bound denoted by the horizontal dot-dashed line [16]. The yellow shaded area corresponds to the region excluded by causality. The two NICER measurements are not included in this figure, since they do not provide additional hard constraints on the  $M - R$  relations.

Ref. [69], while other studies investigating a hadron-quark continuity also found similar results [93]. Recent developments regarding the so-called quarkyonic matter, which unify hadronic and quark matter, produce a similar stiffening [94,95].

As described in Sec. III C, the EoSs are needed to calculate the  $M - R$  curves and  $\Lambda$  tidal deformability parameters for a compact star. In Fig. 4, the  $M - R$  curves can be seen for the EoSs of the SFHo model, of the pure quark model and of hybrid stars with various  $g_V$  vector couplings. We see that, while the low-density (low-mass) behavior of the relations for hybrid stars is determined by the hadronic EoS, the maximum mass region is characterized by the quark EoS. For  $g_V = 0$ , where the hybrid EoS smoothly interpolates between the two phases (see Fig. 3), the quark and hybrid models describe maximum mass compact stars with approximately the same masses. For larger vector couplings, on the other hand, the maximum mass is greatly increased due to the intermediate stiffening of the hybrid EoS. The radii of quark stars with larger vector couplings are also greatly increased, owing to the absence of the first-order phase transition and an incorrect low-density behavior—due to the lack of proper degrees of freedom, i.e., the baryons, at low densities.

In Fig. 5, the tidal deformability parameter versus the compact star mass can be seen for the same EoSs as in the case of Fig. 4. Note that the constraint  $\Lambda(1.4 M_\odot) < 800$

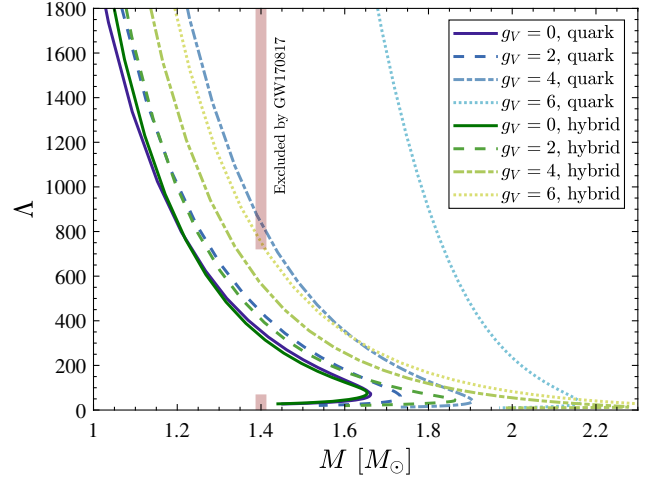


FIG. 5. The same curves as in Fig. 4, but for the tidal deformabilities  $\Lambda$  as function of the compact star masses  $M$ . The red bar corresponds to the region excluded by the constraint  $70 < \Lambda(1.4 M_\odot) < 720$  deduced from the measurement of GW170817 [81].

would correspond to the upper radius constraint of Annala *et al.* [77] on the  $M - R$  plot and would exclude the same models. Currently the measurements of the tidal deformabilities cannot provide stricter constraint on the EoSs than mass and radius measurements; however, both are expected to be improved with upcoming measurements. From the two figures, we can conclude that considering hybrid stars the vector coupling should be in the following range to meet all the requirements,

$$2.5 < g_V < 4.3. \quad (47)$$

This range is valid in case of  $m_\sigma = 290$  MeV and can be directly seen in Fig. 6, in which the maximum mass of stable NSs is shown as a function of  $g_V$  for different  $m_\sigma$ . The lower value of the range is given by the intersection point of the curve with the 95.4% lower bound from PSR J0740 + 6620, while the upper one is from the intersection point of the curve with the top of the light rose-colored band (titled Rezzolla *et al.*)

## B. Dependence on the sigma meson mass

Besides  $g_V$ , there is another very important parameter, the mass of the  $f_0$  or  $\sigma$  meson, that substantially changes the behavior of the solution to the field equations and consequently the behavior of the EoS itself. Its very important role comes from the fact that the  $\sigma_N$  nonstrange and the  $\sigma_S$  strange scalar fields acquire nonzero condensates—which are the  $\phi_N$  and  $\phi_S$ —in the meson sector. However, it is worth noting that other condensates, like pion or kaon condensates, are also considered in the literature; see, e.g., Refs. [96,97], but that is out of the scope of the current investigation. In Fig. 7, one can see

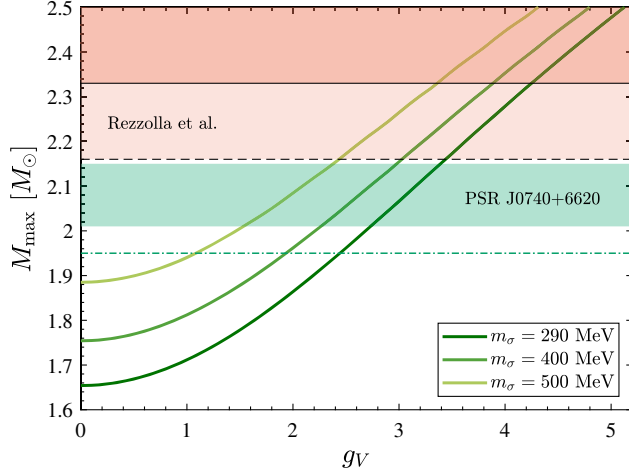


FIG. 6. The maximum mass of stable NS sequences as a function of the vector coupling  $g_V$ , for different sigma masses. The parameters of the concatenation are  $\bar{n} = 3.5n_0$  and  $\Gamma = 1.5n_0$ . For higher sigma masses, this results in EoSs that violate either thermodynamic stability or causality.

the  $\phi_{N/S}$  condensates as a function of the  $\mu_q$  quark chemical potential for different values of  $m_\sigma$ . As can be seen, the phase transition is first order only for very low values of  $m_\sigma$ , which is indicated by the slight back bending of the  $m_\sigma = 290$  MeV curve for  $\phi_{N/S}$ . If  $m_\sigma \gtrsim 300$  MeV, the transition becomes crossover and the pseudocritical chemical potential—defined by the inflection point of the  $\phi_N(\mu_q)$  curve—shifts toward larger values.

The effect of changing  $m_\sigma$  for three different  $g_V$  values can be seen in Fig. 8. It can be observed that generally the

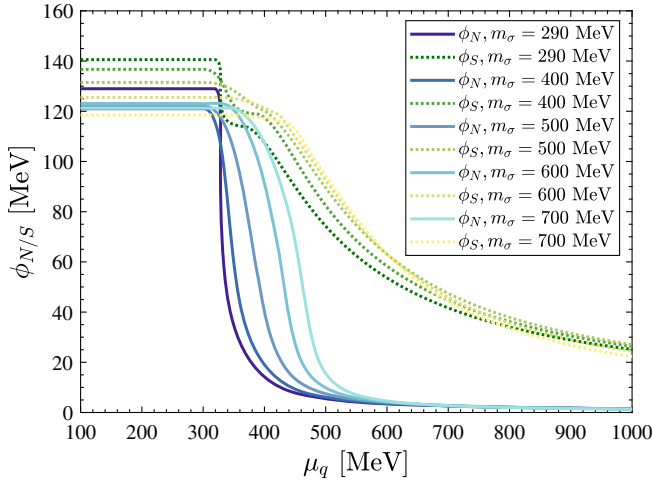


FIG. 7. The chemical potential dependence of the  $\phi_N$  (blue solid) and  $\phi_S$  (green dotted) scalar condensates. Increasingly bright tones correspond to parameter sets with increasing sigma meson masses with  $g_V = 3$  for each curve. For larger  $m_\sigma$  masses, the first-order phase transition [indicated by the slight back bending of the  $\phi(\mu_q)$  curves] disappears, and for  $m_\sigma = 700$  MeV, the vacuum expectation value of  $\phi_N$  becomes larger than the value of  $\phi_S$ .

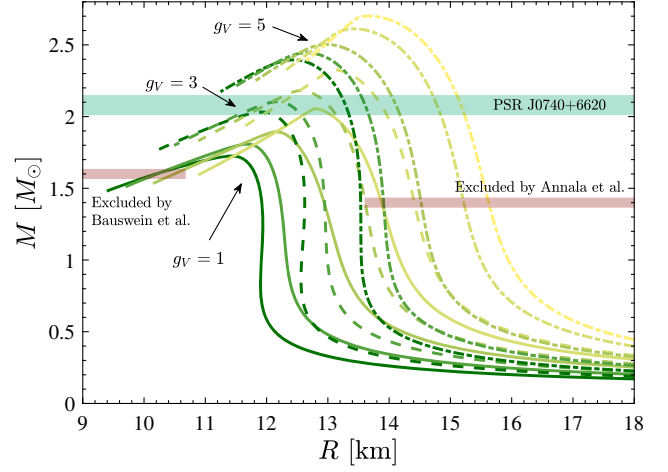


FIG. 8.  $M - R$  relations of hybrid stars for different vector couplings and sigma meson masses, using the SFHo hadronic EoS and the energy density interpolation with  $\bar{n}_B = 3.5n_0$  and  $\Gamma = 2n_0$ . Increasingly bright tones correspond to the five parameter sets with increasing  $m_\sigma$  (the same as in Fig. 7), while the different types of lines correspond to different vector couplings of 1 (solid), 3 (dashed), and 5 (dot-dashed). The curves for  $m_\sigma = 700$  MeV with  $g_V = 1$  and 3 are omitted, since the hybrid EoSs produced with these parameters are not stable.

larger  $m_\sigma$  and  $g_V$  are, the larger the compact star masses and radii are. However, the value of  $m_\sigma$  moderately modifies the slope of the  $M - R$  curve in the midmass region. For a given  $g_V$  value, the change in the value of the maximum mass is about 15%–17% for the total range of the  $\sigma$  mass studied here. On the other hand, if for a fixed  $m_\sigma$  we change  $g_V$  from 1 to 5, we get an approximately 40% change in the maximum mass.

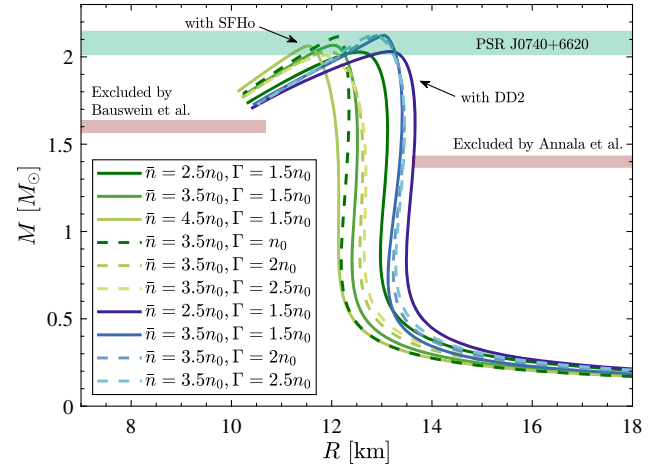


FIG. 9.  $M - R$  relations of hybrid stars with the SFHo (green) and the DD2 (blue) hadronic EoSs and the energy density interpolation method with different values for  $\bar{n}_B$  (solid) and for  $\Gamma$  (dashed). Brighter tones correspond to larger values in both cases.  $g_V = 3$  for each curve. For the DD2 case, only the  $M - R$  curves of stable EoSs are included.

### C. Dependence on hadronic EoS and concatenation method and the role of the bag constant

We also investigated the effects of changing the hadronic EoS and the method of concatenation. In Fig. 9, the  $M - R$  curves are shown for different  $\bar{n}_B$  and  $\Gamma$  values with the SFHo and DD2 hadronic models. Even though the radii of hybrid stars are dependent on the choice of the phase transition parameters and the hadronic EoS, the maximum mass allowed by the different models is encompassed within a small range.

As it is discussed in Sec. III B, two different kinds of interpolation were used in our investigations, one that interpolates between the energy densities as a function

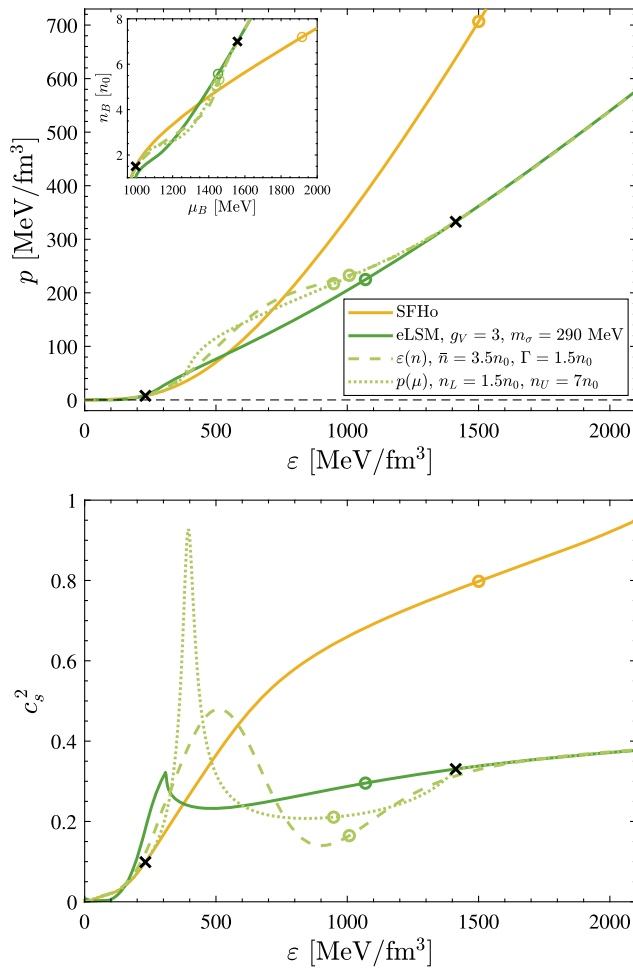


FIG. 10. Top: hybrid EoSs produced by the two concatenation methods using the SFHo model (yellow solid line) and the eLSM with the parameter set corresponding to  $m_\sigma = 290$  MeV and  $g_V = 3$  (green solid line). The black crosses correspond to  $n_L \equiv n_{B,H}(\mu_{BL})$  and  $n_U \equiv n_{B,Q}(\mu_{BU})$ , while the circles correspond to the central conditions inside the maximum mass NSs. The parameters of the two types of interpolation methods were chosen so that both arrive to the hadronic and quark EoSs at approximately the same densities. Bottom: the speed of sound squared for the same EoSs.

of the baryon density and another one that uses the pressure as a function of the baryochemical potential. The comparison of the two approaches can be seen in Fig. 10 for given values of  $g_V$  and  $m_\sigma$ . The  $\varepsilon(n)$  (dashed) and the  $p(\mu)$  (dotted) interpolations both show similar features with stiffenings in the intermediate-density region, although this starts at lower densities for the  $p(\mu)$  case. Even if the two kinds of interpolation methods use very different functions—a polynomial and a tangent hyperbolic—we see similar behavior in the intermediate region. It is also worth noting that, even though the EoSs look similar, more pronounced difference in the speed of sound are apparent for the two different interpolation methods.

In Fig. 11, the effect of the different interpolation methods are shown for the two types of hadronic EoSs, the SFHo, and the DD2. In both cases, there is a slight change in the values of the maximal mass that happens oppositely for the two hadronic EoSs. In the middle-mass range, there is also a slight change in the radii, which act in the same way for the two hadronic curves by increasing the radius, which shows a smaller effect for the case of DD2. With the current observations, neither of the scenarios depicted here can be excluded.

Finally, we have also investigated the role of the bag constant  $B$  in the current framework. We have taken different values for  $B^{1/4}$  from 0 to 110 MeV (similarly to Ref. [32]). The bag constant represents a vacuum contribution, and it is simply an additional constant for the pressure and the energy density.

In Fig. 12, the effect of a nonzero  $B$  term can be seen for the two kinds of interpolation methods. In the upper panel, the  $M - R$  relations for the  $\varepsilon(n)$  concatenation are shown for two  $g_V$  and four  $B^{1/4}$  values. As  $B^{1/4}$  increases, the low mass NSs will develop small radii—as if they were pure

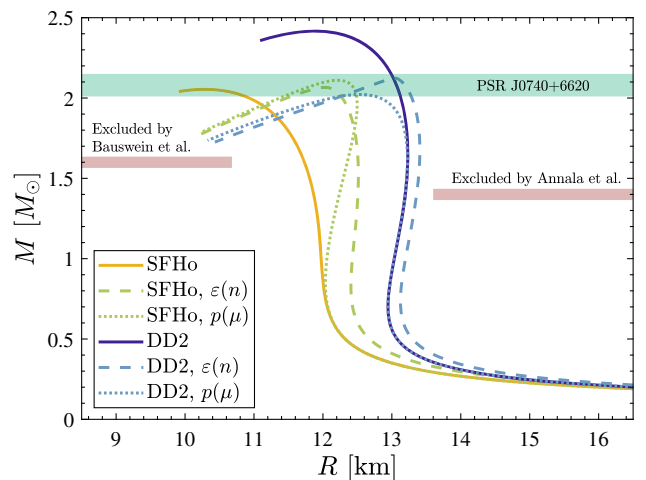


FIG. 11.  $M - R$  relations of hybrid stars for different concatenations as well as for the SFHo (yellow) and DD2 (blue) hadronic EoSs. The parameters for the  $\varepsilon(n)$  (dashed) and  $p(\mu)$  (dotted) concatenations are the same as in Fig. 10.

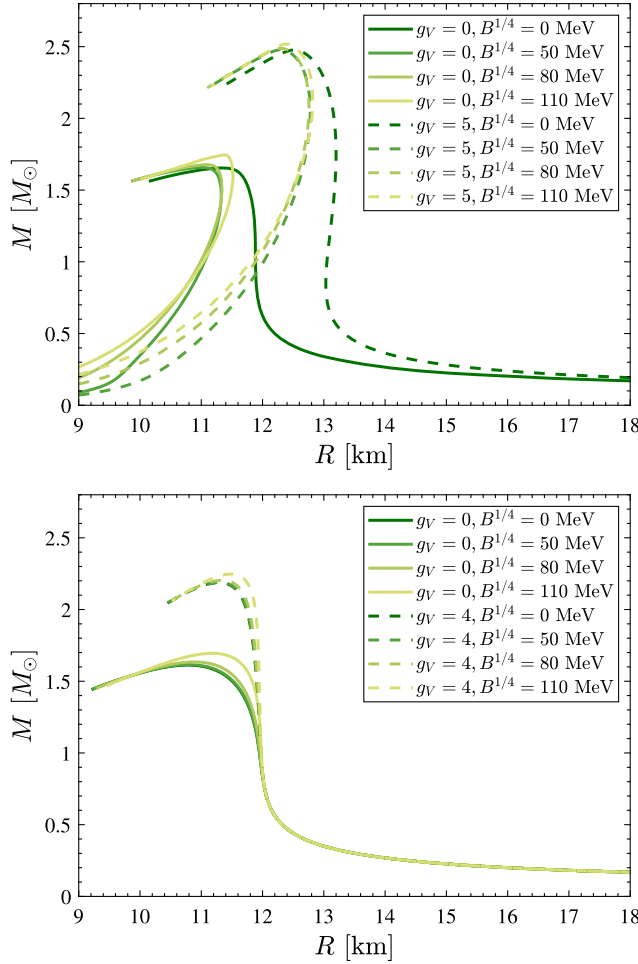


FIG. 12.  $M - R$  relations in case of a nonzero bag constant for the  $\varepsilon(n)$  (top) and the  $p(\mu)$  (bottom) interpolation methods. In the  $p(\mu)$  case, the interpolation limits were chosen so that larger values for  $B$  could be accommodated as well without producing unstable EoSs.

quark stars—due to an incorrect low-density behavior. This happens because in case of the  $\varepsilon(n)$  concatenation the onset of the phase transition does not have a strict starting point and therefore the quarklike behavior can dominate at low densities as well in some cases. Owing to this erroneous behavior, it is advisable to only apply this method with due caution. This behavior cannot be observed in case of the  $p(\mu_B)$  concatenation in the lower panel of Fig. 12. Also, besides this change, the effect of the bag constant is not so dramatic in our case. In Fig. 13, we show  $M - R$  curves for a concatenation in the  $\varepsilon(n)$  plane with the same polynomial method as in the  $p(\mu)$  case, where the previous problem of an incorrect low-density behavior is avoided.

Many previous studies have also investigated the effect of changing the bag constant, only using a Maxwell construction for modeling the phase transition (e.g., Refs. [32,98]). Some of these studies found that the  $M - R$  curves cross each other in the vicinity of a single

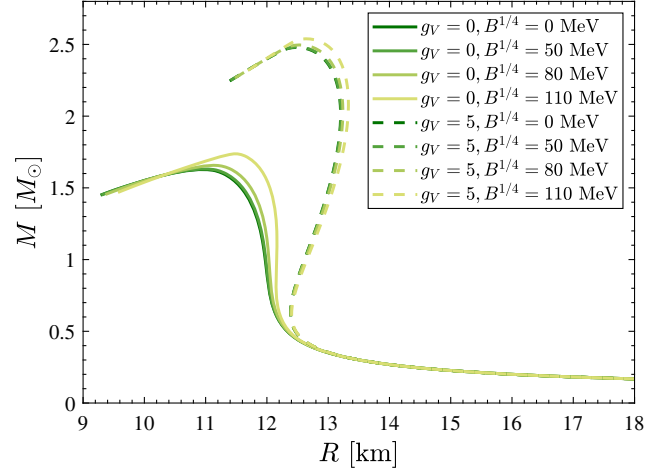


FIG. 13.  $M - R$  relations with various bag constants in case of a polynomial interpolation in  $\varepsilon(n)$ . The interpolation parameters are  $n_L = 1.2n_0$  and  $n_U = 7n_0$ . In this case, the problem with the incorrect low-density behavior is evaded.

point, the so-called special point [98–100]. Even though these studies mostly apply a constant speed-of-sound construction for the quark part, it was also shown that the special point also appears with more realistic EoSs, albeit it gets smeared. Since both our quark EoS and the concatenation methods substantially differ from the model case investigated in these papers, we do not expect an exact special point to appear. Still, a similar feature can be observed in Figs. 12 and 13 on the unstable part of the  $M - R$  curves in case of the polynomial concatenations, although this is also missing for the  $\varepsilon(n)$  concatenation with tangent hyperbolic interpolation.

## V. CONCLUSIONS

We investigated hybrid star properties using the concept of hadron-quark crossover, in which we took a hadronic EoS together with a quark one and connected them with some smooth interpolation method in an intermediate region where both models are inaccurate. For the hadronic EoS, we have used two different relativistic mean field models, the SFHo and the DD2, while for the quark part, a vector and axial-vector meson extended linear sigma model was used with additional constituent quarks. The latter model reproduces the meson spectrum in vacuum well and also agrees with various lattice results at finite temperature and zero density.

We argued that the changes in the values of the parameters of the Lagrangian can have a significant effect on the properties of the EoS and consequently on the properties of hybrid stars themselves. For this very reason, we investigated the asymptotic behavior of our system of equations as a function of the  $\mu_q$  quark chemical potential and found a condition among a set of parameters of our

Lagrangian that should be fulfilled in order to acquire vanishing chiral condensates for very large  $\mu_q$ , as it is expected physically.

The interpolation method was also altered, and its effect on the  $M - R$  curves was shown to be moderate in the midmass range, while the maximum hybrid star mass remained approximately constant. Moreover, the parameters of the interpolation (like position and width), the  $g_V$  vector coupling, and the  $m_\sigma$  sigma meson mass were also changed in some range, and their effects were analyzed in detail. We found that for a given value of the sigma meson mass there is a relatively small acceptable range in  $g_V$ , imposing constraints from astrophysical observations. The consequences of the constraints on the tidal deformabilities for different EoSs and  $g_V$  vector couplings was also discussed. Finally, we found in connection with the bag constant that its introduction does not affect the  $M - R$  curves significantly if its value is not too high for a given  $g_V$  value.

In conclusion, all the current astrophysical constraints from observation are compatible with the investigated phenomenological model if the relevant parameters—like the vector coupling or the sigma meson masses—are within a certain range and the parameters also satisfy a condition that comes from the investigation of the asymptotic behavior of the field equations. Turning the argument around, one sees that data from NSs considerably constrain

the parameters of the chiral quark-meson model for bulk quark matter.

It is worth it to note that the  $g_V$  vector coupling can also be determined from the parametrization procedure if one uses one-loop order curvature masses for the vector and axial vector meson masses [50]. In Ref. [50], its value was found to be around 5 for a sigma mass around 300 MeV, which is a little higher than the upper bound of the acceptable range found here. To resolve this tension, further investigation is needed.

## ACKNOWLEDGMENTS

J. T. and P. K. acknowledge support by the National Research, Development and Innovation (NRDI) fund of Hungary, financed under the FK\_19 funding scheme, Project No. FK 131982. J. T., P. K., and G. W. acknowledge the support of the NRDI fund K138277. P. K. also acknowledges support by the János Bolyai Research Scholarship of the Hungarian Academy of Sciences. J. T. was supported by the UNKP-21-3 New National Excellence Program of the Ministry for Innovation and Technology from the source of NRDI fund. J. S.-B. acknowledges support by the Deutsche Forschungsgemeinschaft (DFG, German Research Foundation), Project No. 315477589-TRR 211. P. K. would also like to thank Zsolt Szép for his valuable comments about the manuscript.

## APPENDIX A: GRAND POTENTIAL IN THE HYBRID APPROXIMATION

The grand potential in the current (hybrid) approximation reads

$$\begin{aligned} \Omega_{\text{tot}} = & \frac{1}{2} m_0^2 (\phi_N^2 + \phi_S^2) + \frac{\lambda_1}{4} (\phi_N^2 + \phi_S^2)^2 + \frac{\lambda_2}{8} (\phi_N^4 + 2\phi_S^4) - \frac{c_1}{2\sqrt{2}} \phi_N^2 \phi_S - h_N \phi_N - h_S \phi_S \\ & - \frac{1}{2} m_\rho^2 (v_\omega^2 + v_\rho^2) - \frac{1}{2} m_\Phi^2 v_\Phi^2 - \frac{3}{8\pi^2} \left[ m_u^4 \log\left(\frac{m_u}{M_0}\right) + m_d^4 \log\left(\frac{m_d}{M_0}\right) + m_s^4 \log\left(\frac{m_s}{M_0}\right) \right] \\ & - \frac{3}{8\pi^2} \sum_{f \in (u, d, s)} m_f^4 \left[ \log\left(\gamma_f + \sqrt{\gamma_f^2 - 1}\right) + \frac{1}{3} \gamma_f \sqrt{\gamma_f^2 - 1} (2\gamma_f^2 - 5) \right] \\ & - \frac{m_e^4}{8\pi^2} \left[ \log\left(\gamma_e + \sqrt{\gamma_e^2 - 1}\right) + \frac{1}{3} \gamma_e \sqrt{\gamma_e^2 - 1} (2\gamma_e^2 - 5) \right], \end{aligned} \quad (\text{A1})$$

where the vector masses are given by

$$m_\rho^2 = m_\omega^2 = m_1^2 + \frac{1}{2} h_1 (\phi_N^2 + \phi_S^2) + \frac{1}{2} (h_2 + h_3) \phi_N^2, \quad (\text{A2})$$

$$m_\Phi^2 = m_1^2 + \frac{1}{2} h_1 (\phi_N^2 + \phi_S^2) + (h_2 + h_3) \phi_S^2 + 2\delta_S, \quad (\text{A3})$$

and

$$\gamma_f = \frac{|\tilde{\mu}_f|}{m_f}, \quad f \in (u, d, s), \quad \gamma_e = \frac{|\mu_e|}{m_e} \quad (\text{A4})$$

have also been introduced.

## APPENDIX B: PARAMETER SETS

In Table III, we present all the parameter sets that were used for the different sigma masses.

TABLE III. Parameter values for different sigma meson masses.

Parameter	$m_\sigma = 400$ MeV	$m_\sigma = 500$ MeV	$m_\sigma = 600$ MeV	$m_\sigma = 700$ MeV
$\phi_N$ (GeV)	0.1210	0.1218	0.1231	0.1212
$\phi_S$ (GeV)	0.1367	0.1315	0.1255	0.1185
$m_0^2$ (GeV <sup>2</sup> )	$-3.5902_{E-2}$	$-8.6251_{E-2}$	-0.1780	-0.2777
$m_1^2$ (GeV <sup>2</sup> )	0.5600	0.5600	0.5600	0.5600
$\lambda_1$	0.1757	0.9634	1.3876	2.3572
$\lambda_2$	23.0159	25.9249	29.7608	34.9895
$c_1$ (GeV)	1.5884	1.6273	1.6407	1.7110
$\delta_S$ (GeV <sup>2</sup> )	0.2371	0.2323	0.2305	0.2351
$g_1$	5.3250	5.4668	5.6116	5.8237
$g_2$	-2.5367	-2.1499	-1.6939	-1.4069
$h_1$	5.3887	3.9904	0.6246	-1.1022
$h_2$	-10.3257	-7.4554	-1.9978	1.4249
$h_3$	1.8646	1.4698	1.0551	0.2283
$g_F$	5.0050	5.0396	5.3835	5.7157
$M_0$ (GeV)	0.4522	0.4522	0.5579	0.6357

- 
- [1] Y. Aoki, G. Endrodi, Z. Fodor, S.D. Katz, and K. K. Szabo, *Nature (London)* **443**, 675 (2006).
- [2] S. Borsanyi, Z. Fodor, C. Hoelbling, S. D. Katz, S. Krieg, and K. K. Szabo, *Phys. Lett. B* **730**, 99 (2014).
- [3] P. de Forcrand, Proc. Sci., LAT2009 (2009) 010.
- [4] A. Kurkela, P. Romatschke, and A. Vuorinen, *Phys. Rev. D* **81**, 105021 (2010).
- [5] A. Grelli (ALICE Collaboration), *EPJ Web Conf.* **171**, 01005 (2018).
- [6] T. Sakaguchi (PHENIX Collaboration), *Proc. Sci., HardProbes2018* (2019) 035 [arXiv:1901.01951].
- [7] D. Tlusty, in *13th Conference on the Intersections of Particle and Nuclear Physics (CIPANP 2018) Palm Springs, California, USA* (2018), arXiv:1810.04767.
- [8] D. T. Larsen (NA61/SHINE Collaborations), *KnE Energy Phys.* **3**, 188 (2018).
- [9] T. Ablyazimov *et al.* (CBM Collaboration), *Eur. Phys. J. A* **53**, 60 (2017).
- [10] V. D. Kekelidze (NICA Collaboration), *J. Instrum.* **12**, C06012 (2017).
- [11] E. Annala, T. Gorda, A. Kurkela, J. Nättilä, and A. Vuorinen, *Nat. Phys.* **16**, 907 (2020).
- [12] D. Blaschke, A. Ayriyan, D. E. Alvarez-Castillo, and H. Grigorian, *Universe* **6**, 81 (2020).
- [13] P. Demorest, T. Pennucci, S. Ransom, M. Roberts, and J. Hessels, *Nature (London)* **467**, 1081 (2010).
- [14] J. Antoniadis *et al.*, *Science* **340**, 6131 (2013).
- [15] H. T. Cromartie *et al.* (NANOGrav Collaboration), *Nat. Astron.* **4**, 72 (2020).
- [16] E. Fonseca *et al.*, *Astrophys. J. Lett.* **915**, L12 (2021).
- [17] B. P. Abbott *et al.* (LIGO Scientific, Virgo Collaborations), *Phys. Rev. Lett.* **121**, 161101 (2018).
- [18] B. P. Abbott *et al.* (LIGO Scientific, Virgo Collaboration), *Astrophys. J. Lett.* **892**, L3 (2020).
- [19] T. E. Riley *et al.*, *Astrophys. J. Lett.* **887**, L21 (2019).
- [20] M. C. Miller *et al.*, *Astrophys. J. Lett.* **887**, L24 (2019).
- [21] T. E. Riley *et al.*, *Astrophys. J. Lett.* **918**, L27 (2021).
- [22] M. C. Miller *et al.*, *Astrophys. J. Lett.* **918**, L28 (2021).
- [23] F. Ozel, D. Psaltis, T. Guver, G. Baym, C. Heinke, and S. Guillot, *Astrophys. J.* **820**, 28 (2016).
- [24] V. A. Dexheimer and S. Schramm, *Phys. Rev. C* **81**, 045201 (2010).
- [25] R. Negreiros, V. A. Dexheimer, and S. Schramm, *Phys. Rev. C* **82**, 035803 (2010).
- [26] V. Dexheimer, J. Steinheimer, R. Negreiros, and S. Schramm, *Phys. Rev. C* **87**, 015804 (2013).
- [27] V. Dexheimer, R. de Oliveira Gomes, S. Schramm, and H. Pais, *J. Phys. G* **46**, 034002 (2019).
- [28] J. Roark and V. Dexheimer, *Phys. Rev. C* **98**, 055805 (2018).
- [29] V. Dexheimer, R. O. Gomes, T. Klähn, S. Han, and M. Salinas, *Phys. Rev. C* **103**, 025808 (2021).
- [30] A. Zacchi, R. Stiele, and J. Schaffner-Bielich, *Phys. Rev. D* **92**, 045022 (2015).

- [31] A. Zacchi, L. Tolos, and J. Schaffner-Bielich, *Phys. Rev. D* **95**, 103008 (2017).
- [32] A. Zacchi and J. Schaffner-Bielich, *Phys. Rev. D* **100**, 123024 (2019).
- [33] K. Otto, M. Oertel, and B.-J. Schaefer, *Phys. Rev. D* **101**, 103021 (2020).
- [34] K. Otto, M. Oertel, and B.-J. Schaefer, *Eur. Phys. J. Special Topics* **229**, 3629 (2020).
- [35] D. E. Alvarez-Castillo, D. B. Blaschke, A. G. Grunfeld, and V. P. Pagura, *Phys. Rev. D* **99**, 063010 (2019).
- [36] M. Shahrbafl, D. Blaschke, A. G. Grunfeld, and H. R. Moshfegh, *Phys. Rev. C* **101**, 025807 (2020).
- [37] D. Blaschke, A. Ayriyan, D. E. Alvarez-Castillo, and H. Grigorian, *Universe* **6**, 81 (2020).
- [38] M. Marczenko, D. Blaschke, K. Redlich, and C. Sasaki, *Astron. Astrophys.* **643**, A82 (2020).
- [39] K. Rajagopal and F. Wilczek, The condensed matter physics of QCD, in *At the Frontier of Particle Physics. Handbook of QCD. Vol. 1-3*, edited by M. Shifman and B. Ioffe (World Scientific, Singapore, 2000), pp. 2061–2151.
- [40] T. Klähn, D. Blaschke, F. Sandin, C. Fuchs, A. Faessler, H. Grigorian, G. Ropke, and J. Trumper, *Phys. Lett. B* **654**, 170 (2007).
- [41] T. Klähn, R. Łastowiecki, and D. B. Blaschke, *Phys. Rev. D* **88**, 085001 (2013).
- [42] G. Baym, T. Hatsuda, T. Kojo, P. D. Powell, Y. Song, and T. Takatsuka, *Rep. Prog. Phys.* **81**, 056902 (2018).
- [43] A. Ayriyan, D. Blaschke, A. G. Grunfeld, D. Alvarez-Castillo, H. Grigorian, and V. Abgaryan, *Eur. Phys. J. A* **57**, 318 (2021).
- [44] D. Parganlija, P. Kovacs, G. Wolf, F. Giacosa, and D. H. Rischke, *Phys. Rev. D* **87**, 014011 (2013).
- [45] P. Kovács, Z. Szép, and G. Wolf, *Phys. Rev. D* **93**, 114014 (2016).
- [46] P. Zyla *et al.* (Particle Data Group), *Prog. Theor. Exp. Phys.* **2020**, 083C01 (2020).
- [47] Y. Aoki, Z. Fodor, S. Katz, and K. Szabó, *Phys. Lett. B* **643**, 46 (2006).
- [48] S. Borsanyi, Z. Fodor, C. Hoelbling, S. D. Katz, S. Krieg, C. Ratti, and K. K. Szabo (Wuppertal-Budapest Collaboration), *J. High Energy Phys.* **09** (2010) 073.
- [49] A. Bazavov *et al.* (HotQCD Collaboration), *Phys. Lett. B* **795**, 15 (2019).
- [50] G. Kovács, P. Kovács, and Z. Szép, *Phys. Rev. D* **104**, 056013 (2021).
- [51] P. Huovinen and P. Petreczky, *Nucl. Phys.* **A837**, 26 (2010).
- [52] A. Bazavov *et al.* (HotQCD Collaboration), *Phys. Rev. D* **86**, 034509 (2012).
- [53] J. E. Lynn, I. Tews, J. Carlson, S. Gandolfi, A. Gezerlis, K. E. Schmidt, and A. Schwenk, *Phys. Rev. Lett.* **116**, 062501 (2016).
- [54] I. Tews, J. Carlson, S. Gandolfi, and S. Reddy, *Astrophys. J.* **860**, 149 (2018).
- [55] I. Tews, J. Margueron, and S. Reddy, *Eur. Phys. J. A* **55**, 97 (2019).
- [56] S. Mogliacci, J. O. Andersen, M. Strickland, N. Su, and A. Vuorinen, *J. High Energy Phys.* **12** (2013) 055.
- [57] M. Oertel, M. Hempel, T. Klähn, and S. Typel, *Rev. Mod. Phys.* **89**, 015007 (2017).
- [58] S. Shlomo, V. M. Kolomietz, and G. Colò, *Eur. Phys. J. A* **30**, 23 (2006).
- [59] J. Piekarewicz, *J. Phys. G* **37**, 064038 (2010).
- [60] L.-W. Chen, C. M. Ko, B.-A. Li, and J. Xu, *Phys. Rev. C* **82**, 024321 (2010).
- [61] B.-A. Li, P. G. Krastev, D.-H. Wen, and N.-B. Zhang, *Eur. Phys. J. A* **55**, 117 (2019).
- [62] A. W. Steiner, M. Hempel, and T. Fischer, *Astrophys. J.* **774**, 17 (2013).
- [63] S. Typel, G. Ropke, T. Klähn, D. Blaschke, and H. Wolter, *Phys. Rev. C* **81**, 015803 (2010).
- [64] M. Hempel and J. Schaffner-Bielich, *Nucl. Phys.* **A837**, 210 (2010).
- [65] G. Baym, C. Pethick, and P. Sutherland, *Astrophys. J.* **170**, 299 (1971).
- [66] J. W. Negele and D. Vautherin, *Nucl. Phys.* **A207**, 298 (1973).
- [67] V. Abgaryan, D. Alvarez-Castillo, A. Ayriyan, D. Blaschke, and H. Grigorian, *Universe* **4**, 94 (2018).
- [68] G. Baym, S. Furusawa, T. Hatsuda, T. Kojo, and H. Togashi, *Astrophys. J.* **885**, 42 (2019).
- [69] K. Masuda, T. Hatsuda, and T. Takatsuka, *Prog. Theor. Exp. Phys.* **2013**, 073D01 (2013).
- [70] R. C. Tolman, *Phys. Rev.* **55**, 364 (1939).
- [71] J. Oppenheimer and G. Volkoff, *Phys. Rev.* **55**, 374 (1939).
- [72] T. Hinderer, *Astrophys. J.* **677**, 1216 (2008).
- [73] T. Damour and A. Nagar, *Phys. Rev. D* **80**, 084035 (2009).
- [74] S. Postnikov, M. Prakash, and J. M. Lattimer, *Phys. Rev. D* **82**, 024016 (2010).
- [75] J. Takátsy and P. Kovács, *Phys. Rev. D* **102**, 028501 (2020).
- [76] B. P. Abbott *et al.* (LIGO Scientific, Virgo Collaborations), *Phys. Rev. Lett.* **119**, 161101 (2017).
- [77] E. Annala, T. Gorda, A. Kurkela, and A. Vuorinen, *Phys. Rev. Lett.* **120**, 172703 (2018).
- [78] E. R. Most, L. R. Weih, L. Rezzolla, and J. Schaffner-Bielich, *Phys. Rev. Lett.* **120**, 261103 (2018).
- [79] B. P. Abbott *et al.* (LIGO Scientific, Virgo Collaborations), *Phys. Rev. Lett.* **121**, 161101 (2018).
- [80] S. De, D. Finstad, J. M. Lattimer, D. A. Brown, E. Berger, and C. M. Biwer, *Phys. Rev. Lett.* **121**, 091102 (2018); **121**, 259902(E) (2018).
- [81] B. P. Abbott *et al.* (LIGO Scientific, Virgo Collaborations), *Phys. Rev. X* **9**, 011001 (2019).
- [82] E. Annala, T. Gorda, E. Katerini, A. Kurkela, J. Nättilä, V. Paschalidis, and A. Vuorinen, *Phys. Rev. X* **12**, 011058 (2022).
- [83] W. Kastaun and F. Ohme, *Phys. Rev. D* **100**, 103023 (2019).
- [84] P. Landry and R. Essick, *Phys. Rev. D* **99**, 084049 (2019).
- [85] C. D. Capano, I. Tews, S. M. Brown, B. Margalit, S. De, S. Kumar, D. A. Brown, B. Krishnan, and S. Reddy, *Nat. Astron.* **4**, 625 (2020).
- [86] T. Dietrich, M. W. Coughlin, P. T. H. Pang, M. Bulla, J. Heinzel, L. Issa, I. Tews, and S. Antier, *Science* **370**, 1450 (2020).
- [87] A. Bauswein, O. Just, H.-T. Janka, and N. Stergioulas, *Astrophys. J. Lett.* **850**, L34 (2017).
- [88] L. Rezzolla, E. R. Most, and L. R. Weih, *Astrophys. J. Lett.* **852**, L25 (2018).

- [89] G. Raaijmakers, S. K. Greif, K. Hebeler, T. Hinderer, S. Nisanke, A. Schwenk, T. E. Riley, A. L. Watts, J. M. Lattimer, and W. C. G. Ho, *Astrophys. J. Lett.* **918**, L29 (2021).
- [90] S. Huth *et al.*, [arXiv:2107.06229](https://arxiv.org/abs/2107.06229).
- [91] S. Ghosh, D. Chatterjee, and J. Schaffner-Bielich, *Eur. Phys. J. A* **58**, 37 (2022).
- [92] P. Kovacs and Z. Szep, *Phys. Rev. D* **75**, 025015 (2007).
- [93] T. Kojo, *Phys. Rev. D* **104**, 074005 (2021).
- [94] L. McLerran and S. Reddy, *Phys. Rev. Lett.* **122**, 122701 (2019).
- [95] K. S. Jeong, L. McLerran, and S. Sen, *Phys. Rev. C* **101**, 035201 (2020).
- [96] T. Herpay and P. Kovacs, *Phys. Rev. D* **78**, 116008 (2008).
- [97] V. Thorsson, M. Prakash, and J. M. Lattimer, *Nucl. Phys.* **A572**, 693 (1994); **A574**, 851(E) (1994).
- [98] M. Cierniak and D. Blaschke, *Eur. Phys. J. Special Topics* **229**, 3663 (2020).
- [99] A. V. Yudin, T. L. Razinkova, D. K. Nadyozhin, and A. D. Dolgov, *Astron. Lett.* **40**, 201 (2014).
- [100] M. Cierniak and D. Blaschke, *Astron. Nachr.* **342**, 819 (2021).